



Acquisition, optimization and interpretation of X-ray computed tomographic imagery: applications to the geosciences

Richard A. Ketcham*, William D. Carlson

Department of Geological Sciences, University of Texas at Austin, Austin, TX 78712, USA

Abstract

High-resolution X-ray computed tomography (CT) is a novel technology ideally suited to a wide range of geological investigations. It is a quick and nondestructive method to produce images that correspond closely to serial sections through an object. Sequential contiguous images are compiled to create three-dimensional representations that can be manipulated digitally to perform efficiently a large array of measurement and visualization tasks. Optimal data acquisition and interpretation require proper selection of scanning configuration, use of suitable X-ray sources and detectors, careful calibration, and attention to origins and modes of artifact suppression. Visualization of CT data typically profits from the ability to view arbitrarily oriented sections through the three-dimensional volume represented by the data, and from the capability to extract features of interest selectively and display perspective views of them using methods of isocontouring or volume rendering. Geological applications include interior examination of one-of-a-kind fossils or meteorites; textural analysis of igneous and metamorphic rocks; geometric description and quantification of porosity and permeability in rocks and soils; and any other application demanding three-dimensional data that formerly required physical serial sectioning. © 2001 Elsevier Science Ltd. All rights reserved.

Keywords: Visualization; Image analysis

1. Introduction

X-ray computed tomography (CT) is an established and rapidly evolving technology of proven value for geological investigations. Because of its origin outside of the earth sciences, the potential for application of CT imagery to geological problems is only beginning to be explored. This article provides the interested geoscientist with an understanding of the rudiments of X-ray CT, how scanning instrumentation and methods can be optimized for particular imaging tasks, and some of the issues that influence proper utilization of CT data,

together with a description of several past and current geologic applications of X-ray CT.

CT provides nondestructive three-dimensional visualization and characterization, creating images that map the variation of X-ray attenuation within objects, which relates closely to density. Because density transitions usually correspond to boundaries between materials or phases, these data are often straightforward and intuitive for the geologist to interpret. The imagery is commonly analogous to data that would be obtained more tediously and laboriously with serial sectioning. Furthermore, because the data are digital, the method lends itself more easily to both quantitative analysis and widespread dissemination.

Two vivid examples of these advantages are found in the fields of paleontology and metamorphic petrology. A serial-sectioning study of a skull of the mammalian ancestor *Thrinaxodon* was undertaken by Fourie (1974).

*Corresponding author. Tel.: 1-512-471-0260; fax: 1-512-471-9425.

E-mail address: richk@maestro.geo.utexas.edu (R.A. Ketcham).

The sample was ground down in 200- μm increments, and at each stage drawings were made and acetate peels were taken, a process that required 2 years to complete. When the results were published (Fourie, 1974), only a small subset of the images that were obtained could be presented, and the specimen had been destroyed. In contrast, a high-resolution CT scan of another *Thrinaxodon* skull was completed by Rowe et al. (1993) in only 6 h, roughly the time it took to complete and fully document a single serial section in the original study, and the sample remains available for further research. Interpretation of the digital data was greatly aided by image-processing software, and all of the collected data were published on a single compact disk (Rowe et al., 1993).

A similar example is provided by studies focused on quantitative analysis of metamorphic textures. Since the 1960s it has been recognized that the sizes and three-dimensional spatial disposition of porphyroblasts in metamorphic rocks contain information about the atomic-scale processes that control crystal nucleation and growth (Kretz, 1966, 1969). Kretz (1993) acquired the requisite data on crystal sizes and locations of garnet by mechanically dissecting a rock using a steel chisel and brush while recording the positions of each of the porphyroblasts found. A total of 91 crystals were located, measured and subsequently analyzed. In contrast, high-resolution X-ray computed tomography has also been used to reveal the locations of garnet porphyroblasts in several rocks (Carlson and Denison, 1992; Denison et al., 1997). Each was scanned in a few hours, and analysis of the data for each rock required only a few weeks, once the computational process was streamlined. Numbers of crystals measured in a single sample ranged up to 12,000; such large numbers are important, because analyses of the statistical tests applied to the data indicate that at least 1000 crystals should be measured to ensure accurate results (Denison et al., 1997, Appendix 1). Furthermore, the rocks remained available for further study, such as electron microprobe analysis of selected crystals (e.g., Chernoff and Carlson, 1997, 1999).

Many similar examples of geological application of high-resolution CT are accumulating as knowledge and utilization of this technology becomes more prevalent. The synopses of recent CT investigations that conclude this article should provide a sense of the breadth and applicability of this technique to geological problems.

1.1. Industrial computed tomography

First developed for widespread use in medicine for the imaging of soft tissue and bone, X-ray CT was subsequently extended and adapted to a wide variety of industrial tasks. These latter developments, which demanded imagery of denser objects across a range of

size classes and resolution requirements, provided key advances that greatly enhanced the potential for application of this technology to geological investigations.

To maximize their effectiveness in differentiating tissues while minimizing patient exposure, medical CT systems need to use a limited dose of relatively low-energy X-rays ($\leq 125 \text{ keV}$). To obtain as much data as possible given these requirements, they use relatively large (mm-scale), high-efficiency detectors. Because industrial CT systems face no limitations on acceptable radiation dose, they are able to take advantage of several optimizations. X-rays for industrial systems can be of higher energy, and exposure times have no firm upper limit. Smaller detectors can be used, which leads to higher resolution because the decline in signal that accompanies smaller surface area can be compensated by higher X-ray intensities or exposure times. Finally, because the objects being scanned are inanimate, more accurate and precise positioning is possible.

CT scanners can be generally grouped into four categories, based on their spatial resolution and the size of objects they are most suitable for scanning. A proposed classification is summarized in Table 1. Most medical systems fall into the category of conventional CT, although some specialized systems for scanning appendages could be termed high resolution. Industrial scanners can span a wide range of scales, from conventional or larger for scanners designed to image large objects such as engine blocks, down to ultra-high resolution. To achieve the resolution requirements for micro-CT, synchrotron X-ray sources are required (e.g., Coker et al., 1996; Flannery et al., 1987; Kinney et al., 1993). The University of Texas (UT) high-resolution X-ray CT Facility houses a tandem scanner, with both a high-resolution system and an ultra-high-resolution system. Each is described in detail in a later section.

1.2. Geological applications

The natural application of X-ray CT to paleontology was quickly recognized (Conroy and Vannier, 1984). Although medical scanners were able to obtain only low-resolution data on a limited subset of specimens, the fact that CT could acquire interior information

Table 1
General classification of computed tomography

Type	Scale of observation	Scale of resolution
Conventional	m	mm
High-resolution	dm	100 μm
Ultra-high-resolution	cm	10 μm
Microtomography	mm	μm

nondestructively from irreplaceable specimens made it a valuable technique nonetheless (Haubitz et al., 1988). Similarly, CT was also applied to meteorites at an early stage to facilitate study of one-of-a-kind specimens (Arnold et al., 1982). Other successful early geological applications of X-ray CT using medical scanners include investigations in fluid flow, soil science, and sedimentology. Petroleum engineers used CT data to study two-fluid coreflood experiments in reservoir lithologies (Wellington and Vinegar, 1987; Withjack, 1988), and those techniques were later adapted to imaging air sparging as used in environmental remediation (Chen et al., 1996). CT data have been exploited to examine soil transport properties, through both direct imaging of fluid-flow experiments (Anderson et al., 1992; Heijs et al., 1995) and characterization of soil and pore-space morphology (Peyton et al., 1992; Zeng et al., 1996). Medical CT data have also been applied to offshore sediments for characterization of morphology (Orsi and Anderson, 1995; Orsi et al., 1994) and density distribution (Amos et al., 1996). Scale models of faulting have also been studied using medical CT systems, which have become fast enough to allow real-time analysis (Schreurs and Hänni, 1998).

High-resolution industrial X-ray CT allows many of these inquiries to be conducted more effectively by generating much finer-detailed imagery. Paleontological investigations have moved from imaging gross structures to imaging such fine details as tooth replacement in marsupials (Cifelli and Muizon, 1998a; Cifelli and Muizon, 1998b; Cifelli et al., 1996) and inner-ear structure in early mammals (Rowe, 1996). Meteorite investigations have progressed from solely finding inclusions to mapping out the shape and size distributions of their mineralogical components, providing textural clues about their origins (Kuebler et al., 1999). Scans of soil and sediment cores are capable of imaging individual pores and fractures at much higher resolutions (better by an order of magnitude or more than achievable with medical scanners), enabling more detailed research into solute and tracer transport description and modeling (Moline et al., 1997). High-resolution CT has also allowed more detailed analysis of scale models depicting faulting and salt flow (Le Calvez and Vendeville, 1999).

High-resolution imagery has also expanded the breadth of X-ray CT usage to other geologic subdisciplines. One of the first examples was the quantitative textural analysis of porphyroblast crystallization in metamorphic rocks to determine atomic-scale processes controlling nucleation and growth (Carlson and Denison, 1992; Denison and Carlson, 1997; Denison et al., 1997). More recent and ongoing textural investigations include studies of flow pathways for melt in migmatites (Brown et al., 1999) and mingling of different melt types in lamprophyres (Ogasawara et al., 1998). High-

resolution CT is also being used to study spiral inclusion trails in garnet, where the nondestructive acquisition of data for large volumes of rock allows these features to be compared among adjacent garnets and linked to surrounding three-dimensional rock texture and garnet morphology (Bauer et al., 1998). CT analysis to determine the size distribution and morphology of vesicles in basalt has provided new clues to the physics of eruption processes (Proussevitch et al., 1998). Imagery of fractures and pore spaces in reservoir limestone has improved understanding of the geometrical components of porosity and permeability, and their relation to geological and biological features (Beall et al., 1996; Gournay and Kirkland, 1998).

2. Essentials of computed tomography

Because industrial X-ray CT scanners are typically custom-built, it is impossible to provide a detailed description of their principles and operation that will apply in all cases. Instead, we provide here a description of each component of the CT-scanning process, both in general terms and as specifically applied at the University of Texas High-Resolution X-ray CT Facility. The material presented in this and subsequent sections is a combination of information provided with the UT system by the manufacturer (Bio-Imaging Research, Inc., of Lincolnshire, Illinois), insights gained from experience, and general principles derived from the literature. For a more complete technical overview of CT, we recommend ASTM publication E1441-92a (ASTM, 1992) as an excellent starting point. Very readable, if somewhat dated, synopses of medical CT and its components and history can be found in Hendee (1979) and Newton and Potts (1981), the latter of which provides considerable detail about many fundamentals of tomographic scanning.

2.1. Scanning configuration

The simplest common elements of X-ray radiography are an X-ray source, an object to be imaged through which the X-rays pass, and a series of detectors that measure the extent to which the X-ray signal has been attenuated by the object (Fig. 1). A single set of X-ray intensity measurements on all detectors for a given object position and scanner geometry is termed a *view*. The fundamental principle behind computed tomography is to acquire multiple sets of views of an object over a range of angular orientations. By this means, additional dimensional data are obtained in comparison to conventional X-radiography, in which there is only one view. These data are used to create two-dimensional images that are called *slices* because they correspond to

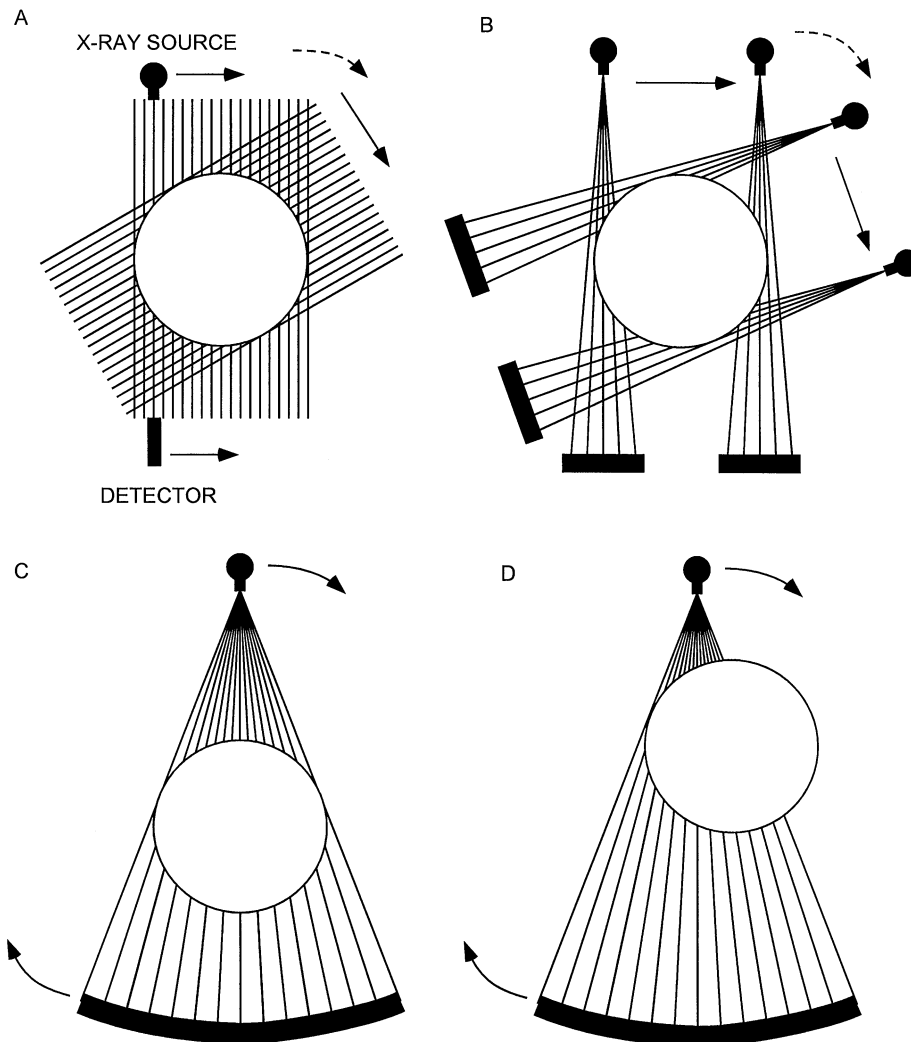


Fig. 1. Schematic illustration of different generations of X-ray CT scan geometries. Solid arrows indicate movements during data collection, dashed arrows indicate movement between sequences of data collection. Solid lines passing from sources to detectors are ray paths, and each set of solid lines from a single angular orientation constitutes a view. These illustrations show the source and detectors moving around stationary object, as is the case with medical scanners. Motion is relative, however, and in many industrial scanners the object moves while the source and detectors are stationary. In all cases, axis of rotation is center of circle. (A) first-generation, translate-rotate pencil beam geometry; (B) second-generation, translate-rotate fan beam geometry; (C) third-generation, rotate-only geometry; (D) third-generation offset-mode geometry.

what would be seen if the object were sliced along the scan plane.

First- through fourth-generation computed tomography systems utilize only rays that are in the scan plane. In first-generation CT (Fig. 1A) this is done by directing a pencil beam through the object to a single detector, translating the source-detector pair across the extent of the object in the scan plane, then repeating the procedure from a number of angular orientations. Second-generation CT (Fig. 1B) uses the same scanning procedure, but a fan beam replaces the pencil beam and

the single detector is replaced by a linear or arcuate series of detectors, leading to a higher rate of data acquisition. In typical third-generation CT (Fig. 1C), the fan beam and detector series are wide enough to encompass the entire object, and thus only rotation of the object or the source-detector combination is required. One variation of third-generation scanning offsets the sample from the center of the fan beam so that a part of it is outside of the beam, but the center of rotation is within it (Fig. 1D). As the object rotates, all of it passes through the fan beam, which permits

reconstruction of a complete image. This technique allows larger objects to be scanned and permits smaller objects to be moved closer to the source into a narrower section of the fan beam, leading to increased resolution through enhanced utilization of detectors to image smaller subsections of the object in any one view. Third-generation scanning tends to be much faster than second-generation, as X-rays are utilized more efficiently. Most modern medical scanners are fourth-generation devices, consisting of a fixed complete ring of detectors and a single X-ray source that rotates around the object being scanned. In first- through third-generation scanners the motion between the object being scanned and the source–detector pair is relative, and can be accomplished either by keeping the object stationary and moving the source–detector pair, as is done in medical CT systems, or vice versa as is more common in industrial systems.

In volume CT, a cone beam or highly collimated, thick, parallel beam is used rather than a fan beam, and a planar grid replaces the linear series of detectors. This allows for much faster data acquisition, as the data required for multiple slices can be acquired in one rotation. However, it is also computationally more intensive, prone to distortion, and in many cases provides lower-resolution images. Whereas volume CT has been largely perfected for some of the most advanced medical systems, and is ideally suited for tomography using synchrotron radiation, for industrial scanners it does not yet provide the same quality of imagery as single-slice arrangements.

The UT facility is capable of second- and third-generation scanning on the high-energy system, and third generation and volume scanning on the ultra-high-resolution system. On each system, however, third-generation scanning is usually the method of choice.

2.2. X-ray source

The important variables that determine how effective an X-ray source will be for a particular task are the size of the focal spot, the spectrum of X-ray energies generated, and the X-ray intensity. The focal-spot size partially defines the potential spatial resolution of a CT system by determining the number of possible source–detector paths that can intersect a given point in the object being scanned. The more such source–detector paths there are, the more blurring of features there will be. The energy spectrum defines the penetrative ability of the X-rays, as well as their expected relative attenuation as they pass through materials of different density. Higher-energy X-rays penetrate more effectively than lower-energy ones, but are less sensitive to changes in material density and composition. The X-ray intensity directly affects the signal-to-noise ratio and thus image

clarity. Higher intensities improve the underlying counting statistics, but often require a larger focal spot.

Many conventional X-ray tubes have a dual filament that provides two focal-spot sizes, with the smaller spot size allowing more detailed imagery at a cost in intensity. Medical CT systems tend to have X-ray spot sizes that range from 0.5 to 2 mm. The high-resolution system at the UT CT Facility utilizes a dual-spot 420-kV X-ray source (Pantak HF420), with spot sizes of 0.8 and 1.8 mm. The small spot has a maximum load of 800 W (i.e., 2 mA at 400 kV), whereas the large spot has a maximum load of 2000 W. The 200 kV tube used for ultra-high resolution work (Feinfocus FXE-200.20) has an adjustable focal spot with a minimum size of $<10\ \mu\text{m}$ at 8 W total load, but at higher loads the spot size is automatically increased to prevent thermal damage to the target. In most cases a slightly “defocused” beam (larger spot size) can be used to improve counting statistics with little cost in resolution. Both sources have tungsten targets.

The energy spectrum generated is usually described in terms of the peak X-ray energy (keV or MeV), but actually consists of a continuum in which the level with maximum intensity is typically less than half of the peak (Fig. 2). The total “effective” spectrum is determined by a number of factors in addition to the energy input of the X-ray source itself, including autofiltering both by absorption of photons generated beneath the surface of a thick target (Silver, 1994) and by passage through the

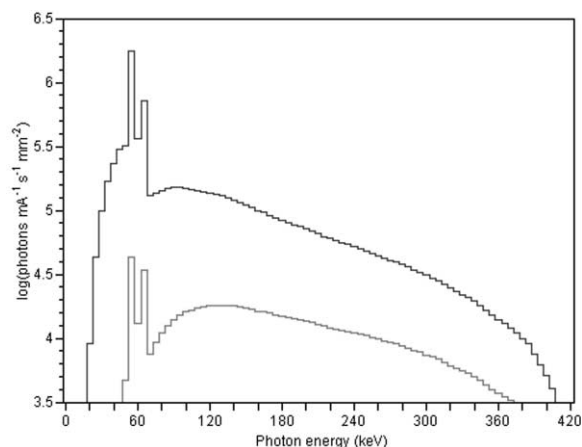


Fig. 2. Theoretical energy spectra for 420-kV X-ray source with tungsten target, calculated combining 5-keV intervals. Spectra consist of continuous *Bremsstrahlung* and characteristic K-series peaks at 57–59 and 67–69 keV. Upper spectrum is modified only by inherent beam filtration by 3 mm of aluminum at tube exit port. Mean X-ray energy is 114 keV. Lower curve represents spectrum that has also passed through 5 cm of quartz. Preferential attenuation of low-energy X-rays causes average energy to rise to 178 keV.

tube exit port; other beam filtration introduced to selectively remove low-energy X-rays; beam hardening in the object being scanned; and the relative efficiency of the detectors to different energies. As discussed below, changes in the X-ray spectrum caused by passage through an object can lead to a variety of scanning artifacts unless efforts are made to compensate for them.

2.3. X-ray attenuation

As the X-rays pass through the object being scanned, the signal is attenuated by scattering and absorption. The basic equation for attenuation of a monoenergetic beam through a homogeneous material is Beer's Law

$$I = I_0 \exp[-\mu x], \quad (1)$$

where I_0 is the initial X-ray intensity, μ is the linear attenuation coefficient for the material being scanned, and x is the length of the X-ray path through the material. If the scan object is composed of a number of different materials, the equation becomes:

$$I = I_0 \exp \left[\sum_i (-\mu_i x_i) \right], \quad (2)$$

where each increment i reflects a single material with attenuation coefficient μ_i over a linear extent x_i . To take into account the fact that the attenuation coefficient is a strong function of X-ray energy, the complete solution would require solving the equation over the range of the effective X-ray spectrum

$$I = \int I_0(E) \exp \left[\sum_i (-\mu_i(E) x_i) \right] dE, \quad (3)$$

However, such a calculation is usually problematical for industrial CT, as the precise form of the X-ray spectrum, and its variation at off-center angles in a fan or cone beam, is usually only estimated theoretically rather than measured. Furthermore, most reconstruction strategies solve Eq. (2), insofar as they assign a single value to each pixel rather than some energy-dependent range.

There are three dominant physical processes responsible for attenuation of an X-ray signal: photoelectric absorption, Compton scattering, and pair production. Photoelectric absorption occurs when the total energy of an incoming X-ray photon is transferred to an inner electron, causing the electron to be ejected. In Compton scattering, the incoming photon interacts with an outer electron, ejecting the electron and losing only a part of its own energy, after which it is deflected in a different direction. In pair production, the photon interacts with a nucleus and is transformed into a positron-electron pair, with any excess photon energy transferred into kinetic energy in the particles produced.

In general for geological materials, the photoelectric effect is the dominant attenuation mechanism at low

X-ray energies, up to approximately 50–100 keV. Compton scatter is dominant at higher energies up to 5–10 MeV, after which pair production predominates. Thus, unless higher-energy sources are used, only photoelectric absorption and Compton scattering need to be considered. The practical importance of the distinction between mechanisms is that photoelectric absorption is proportional to Z^{4-5} , where Z is the atomic number of an atom in the attenuating material, whereas Compton scattering is proportional only to Z (Markowicz, 1993). As a result, low-energy X-rays are more sensitive to differences in composition than higher-energy ones.

The best way to gain insight into what one might expect when scanning a geological sample is to plot the linear attenuation coefficients of the component materials over the range of the available X-ray spectrum. These values can be calculated by combining experimental results for atomic species (e.g., Markowicz, 1993). Alternatively, mass attenuation coefficients can be obtained from the XCOM database managed by NIST (which can be accessed at <http://physics.nist.gov/PhysRefData/Xcom/Text/XCOM.html>). Mass attenuation coefficients must be multiplied by mass density to determine linear attenuation coefficients. To illustrate, Fig. 3 shows curves for four minerals: quartz, orthoclase, calcite, and almandine garnet. Quartz and orthoclase are very similar in mass density (2.65 g/cm³ vs. 2.59 g/cm³), but at low energy their attenuation coefficients are quite different because of the presence of relatively high- Z potassium in the feldspar. With rising X-ray energy, their attenuation coefficients converge,

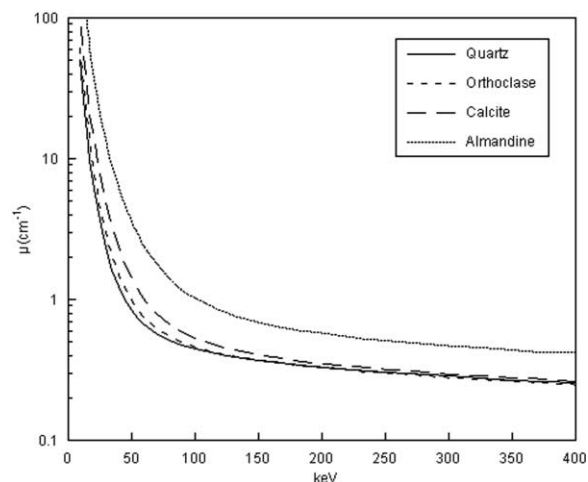


Fig. 3. Linear attenuation coefficient as function of X-ray energy for four rock-forming minerals. Such curves, when combined with the X-ray spectrum utilized for scanning (Fig. 2), allow prediction of ability to differentiate between minerals in CT images.

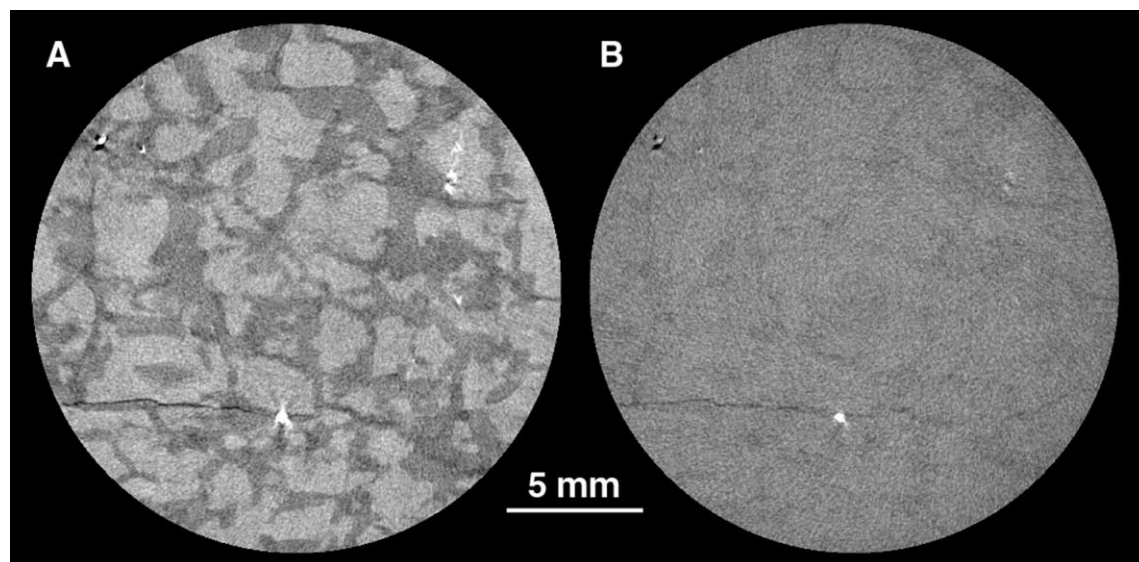


Fig. 4. Core of graphic granite imaged at various energy conditions. Field of view diameter for each image is 22 mm, and slice thickness is 100 μm . Scan (A) was created using X-ray energy of 100 keV and no beam filtration; scan (B) was acquired with X-ray energy of 200 keV and 1/8" brass filter. Both scans employed "self-wedge" calibration.

and at approximately 125 keV they cross; above ~ 125 keV quartz is slightly (but probably indistinguishably) more attenuating, owing to its higher density. Thus, one would expect that these two minerals could be differentiated in CT imagery if the mean X-ray energy used is low enough, but at higher energies they would be nearly indistinguishable (Fig. 4). Calcite, though only slightly denser (2.71 g/cm^3) than quartz and orthoclase, is substantially more attenuating, owing to the presence of calcium. Here the divergence with quartz persists to slightly higher energies, indicating that it should be possible to distinguish the two even on higher-energy scans. High-density, high-Z phases such as almandine are distinguishable at all energies from the other rock-forming minerals examined here.

2.4. X-ray detectors

Detectors for CT scanners make use of scintillating materials in which incoming X-rays produce flashes of light that are counted. Detectors influence image quality through their size and quantity, and through their efficiency in detecting the energy spectrum generated by the source. The size of an individual detector determines the amount of an object that is averaged into a single intensity reading, while the number of detectors determines how much data can be gathered simultaneously. In third-generation scanning, the number of detectors also defines the degree of resolution possible in a single view, and thus in an image overall. The film used in conventional X-ray radiography is an excellent

detector in that it consists, in essence, of a very large number of small and sensitive detectors. Unfortunately, it is not amenable to quickly producing the digital data needed for computed tomography.

The efficiency of scintillation detectors varies with X-ray energy, precisely because higher-energy X-rays are more penetrative than lower-energy ones, indicating that they are more capable of traveling through materials without interactions. This factor must be taken into account when determining the level of expected signal after polychromatic X-rays pass through materials.

The high-resolution system at UT has two separate detectors. The P250D detector consists of a linear array of 512 discrete cadmium tungstate scintillators with dimensions $0.25 \text{ mm} \times 5.0 \text{ mm} \times 5.0 \text{ mm}$, packed in a comb to prevent crosstalk between channels, and each connected to a Si photodiode. Its channel-to-channel pitch is 381 μm , and its total horizontal extent is 195 mm. The RLS (Radiographic Line Scanner) detector consists of a single 0.25-mm thick gadolinium oxysulfide scintillator screen connected to a 2048-channel linear photodiode array using a fiber optic taper. The detector spacing is 50 μm , and the total detector extent is approximately 100 mm. The ultra-high-resolution scanner uses a 9-in image intensifier (Toshiba AI-5764-HVP) as a detector. The image intensifier consists of a partial sphere of cesium iodide scintillators attached to a photocathode. The signal from the photocathode is electronically focused onto a phosphor screen, producing a real-time X-ray image. The image on the phosphor is converted to digital data using a CCD

video system. The video signal, consisting of scan lines divided into pixels, is used to create a set of 512 virtual detectors by software.

3. Acquisition of CT Data

3.1. Sample preparation

Strictly speaking, the only preparation that is absolutely necessary for CT scanning is to ensure that the object fits inside the field of view and that it does not move during the scan. Because the full scan field for CT is a cylinder (i.e., a stack of circular fields of view), the most efficient geometry to scan is also a cylinder. Thus, when possible it is often advantageous to have the object take on a cylindrical geometry, either by using a coring drill or drill press to obtain a cylindrical subset of the material being scanned, or by packing the object in a cylindrical container with either X-ray-transparent filler or with material of similar density. For some applications the sample can also be treated to enhance the contrasts that are visible. Examples have included injecting soils and reservoir rocks with NaI-laced fluids to reveal fluid-flow characteristics (Wellington and Vinegar, 1987; Withjack, 1988), injecting sandstones with Woods metal to map out the fine-scale permeability, and soaking samples in water to bring out areas of differing permeability, which can help to reveal fossils (Zinsmeister and De Nooyer, 1996).

3.2. Calibration

Calibrations are necessary to establish the characteristics of the X-ray signal as read by the detectors under scanning conditions, and to reduce geometrical uncertainties. The latter calibrations vary widely among scanners; as a rule flexible-geometry scanners such as the one at the University of Texas require them, whereas fixed-geometry scanners geared towards scanning a single object type may not.

The two principal signal calibrations are *offset* and *gain*, which determine the detector readings with X-rays off, and with X-rays on at scanning conditions, respectively. An additional signal calibration, called a *wedge*, used on some third-generation systems (including the UT facility) consists of acquiring X-rays as they pass through a calibration material over a 360° rotation. The offset-corrected average detector reading is then used as the baseline from which all data are subtracted. If the calibration material is air, the wedge is equivalent to a gain calibration. A typical non-air wedge is a cylinder of material with attenuation properties similar to those of the scan object. Such a wedge can provide automatic corrections for both beam hardening and ring artifacts (described later), and can allow utilization of high X-ray

intensities that would saturate the detectors during a typical gain calibration. Although widely employed in medical systems, which use phantoms of water or water-equivalent plastic to approximate the attenuating properties of tissue, the wedge calibration is relatively uncommon in industrial systems.

3.3. Collection

The principal variables in collection of third-generation CT data are the number of views and the signal-acquisition time per view. In most cases, rotation is continuous during collection. At the UT CT Facility, the number of views used ranges from 600 to 3600 or more. Each view represents a rotational interval equal to 360° divided by the total number of views. The raw data are displayed such that each line contains a single set of detector readings for a view, and time progresses from top to bottom. This image is called a sinogram, as any single point in the scanned object corresponds to a sinusoidal curve. Second-generation CT data are collected at a small number of distinct angular positions (such as 15 or 30), but the progression of relative object and source-detector position combinations allows these data to complete a fairly continuous sinogram.

3.4. Reconstruction

Reconstruction is the mathematical process of converting sinograms into two-dimensional slice images. The most widespread reconstruction technique is called filtered backprojection, in which the data are first convolved with a filter and each view is successively superimposed over a square grid at an angle corresponding to its acquisition angle. The primary convolution filter used at UT is the Laks filter (Ramachandran and Lakshminarayanan, 1970), which is preferred when high-resolution images are desired; also available is the Shepp-Logan filter (Shepp and Logan, 1974), which is used more frequently in medical systems and reduces noise at some expense in spatial resolution (ASTM, 1992).

During reconstruction, the raw intensity data in the sinogram are converted to *CT numbers* or *CT values* that have a range determined by the computer system. The most common scale used to date has been 12-bit, in which 4096 values are possible. On most industrial scanners, these values correspond to the grayscale in the image files created or exported by the systems. Although CT values should map linearly to the effective attenuation coefficient of the material in each voxel, the absolute correspondence is arbitrary. Medical systems generally use the Hounsfield Unit (HU), in which air is given a CT number of −1000 and water is given a value of 0, causing most soft tissues to have values ranging from −100 to 100 and bone to range from 600 to over 2000 (Zatz, 1981). Industrial CT systems are sometimes

calibrated so that air has a value of 0, water of 1000, and aluminum of 2700, so the CT number corresponds roughly with density (Johns et al., 1993). The calibration of CT values is straightforward for fixed-geometry, single-use systems, but far less so for systems with flexible geometry and scanning modes, and multiple uses each requiring different optimization techniques.

Although a link to a reference scale can be useful in some circumstances, the chemical variability of geological materials and the wide range of scanning conditions used precludes any close correspondence to density in most cases. Furthermore, because material components can range from air to native metals, a rigid scale would be counterproductive. Given the finite range of CT values, a single scale may be insufficiently broad if there are large attenuation contrasts, or needlessly desensitize the system if subtle variations are being imaged. For geological purposes, it is commonly more desirable to select the reconstruction parameters to maximize the CT-value contrast for each scanned object. This can be done by assigning arbitrary low and high values near the limits of the available range to the least and most attenuating features in the scan field. In general we try to ensure that no CT value is generated beyond either end of the 12-bit range, lest some dimensional data be lost. For example, the boundary of an object being scanned in air is usually taken to correspond to the CT-value average between the object and air. If air is assigned to a CT value below zero, the apparent boundary of the object may shift inward.

Two parameters can be used to define a linear conversion between scanner output and the CT value range, corresponding to a slope m and an intercept b . The intercept defines the CT value that the wedge calibration material will have in the final image. Given an initial image with reconstruction parameters m_1 and b_1 , minimum and maximum CT values of $g_{\min 1}$ and $g_{\max 1}$, and desired minimum and maximum CT values of $g_{\min 2}$ and $g_{\max 2}$, the appropriate parameters m_2 and b_2 are:

$$m_2 = m_1(g_{\max 2} - g_{\min 2}) / (g_{\max 1} - g_{\min 1}), \quad (4)$$

$$b_2 = g_{\min 2} - m_2(g_{\min 1} - b_1) / m_1. \quad (5)$$

Care should also be taken to establish CT values for features of interest that may not be directly represented in the scan images. For example, in pore and fracture analysis the CT value of air or water commonly must be known, even if there is no void space large enough to allow this CT value to be achieved in an image.

4. Artifacts and partial volume effects

Although the output of computed tomography is visual in nature and thus lends itself to straightforward

interpretation, subtle complications can render the data more problematic for quantitative use. Scanning artifacts can obscure details of interest, or cause the CT value of a single material to change in different parts of an image. Partial-volume effects, if not properly accounted for, can lead to erroneous determinations of feature dimensions and component volume fractions. In this section we discuss commonly encountered problems, and some approaches for solving them.

4.1. Beam hardening

The most frequently encountered artifact in CT scanning is beam hardening, which causes the edges of an object to appear brighter than the center, even if the material is the same throughout (Fig. 5a). The artifact derives its name from its underlying cause — the increase in mean X-ray energy, or “hardening” of the X-ray beam as it passes through the scanned object. Because lower-energy X-rays are attenuated more readily than higher-energy X-rays, a polychromatic beam passing through an object preferentially loses the lower-energy parts of its spectrum. The end result is a beam that, though diminished in overall intensity, has a higher average energy than the incident beam (Fig. 2). This also means that, as the beam passes through an object, the effective attenuation coefficient of any material diminishes, thus making short ray paths proportionally more attenuating than long ray paths. In X-ray CT images of sufficiently attenuating material, this process generally manifests itself as an artificial darkening at the center of long ray paths, and a corresponding brightening near the edges. In objects with roughly circular cross sections this process can cause the edge to appear brighter than the interior, but in irregular objects it is commonly difficult to differentiate between beam hardening artifacts and actual material variations.

Beam hardening can be a pernicious artifact because it changes the CT value of a material (or void) depending upon its location in an image. Thus, the attempt to utilize a single CT number range to identify and quantify the extent of a particular material can become problematic. One measure that is sometimes taken is to remove the outer edges of the image and analyze only the center. Although this technique removes the worst part of the problem, the artifact is continuous and thus even subsets of the image are affected. Furthermore, if the cross-sectional area of the object changes from slice to slice, the extent of the beam-hardening artifact also changes, making such a strategy prone to error.

There are a number of possible remedies for beam hardening, ranging from sample and scanning preparation to data processing. The simplest approach is to use an X-ray beam that is energetic enough to ensure that beam hardening is negligible, and can thus be ignored. Unfortunately, most materials of geological interest are

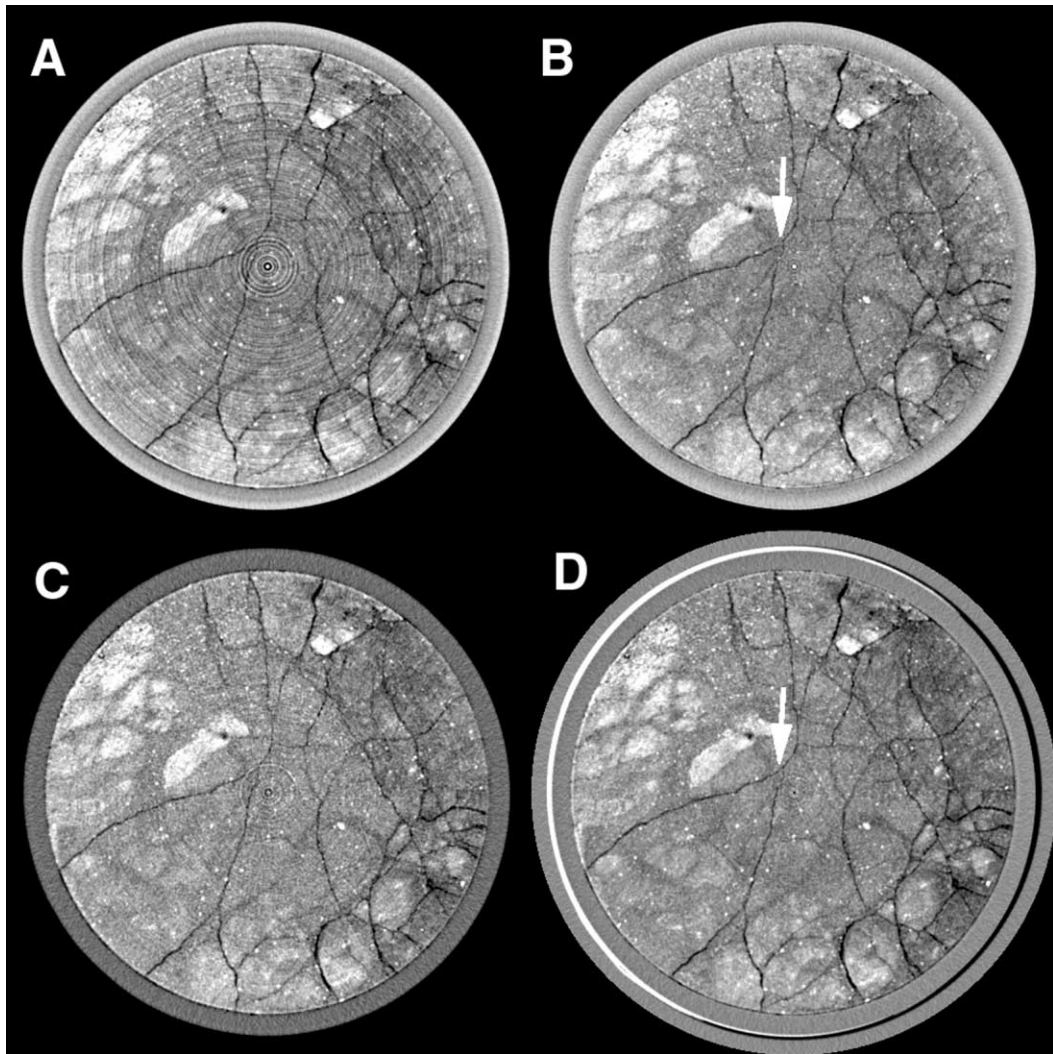


Fig. 5. Scans through 6-in diameter column of saprolite encased in PVC pipe, showing scanning artifacts and results of various strategies for remedying them. Scans all represent 1-mm thick slices collected with X-ray source at 420 kV and acquisition times of 3 min. Scan (A) shows both ring- and beam-hardening artifacts. Latter is visible most obviously as bright ring around outer part of PVC. Image (B) is result of software correction of ring artifacts in (A). If gray-scale fluctuations caused by rings are smaller than for features of interest, this approach can be very successful. However, in this case some fractures close to center have been obscured or altered. Image (C) shows the result of pre-filtering the X-ray beam by passing it through 6.35 mm of brass. Beam-hardening and ring artifacts have been reduced markedly but not totally, and image noise has increased considerably. Scan shown in (D) was done using self-wedge calibration through relatively homogeneous portion of column. Bright rim on left was caused by imperfect centering of column; image of saprolite itself, however, has only very minor ring artifacts and no beam hardening. Note that although centers of images (B) and (D) are similar, edges of the saprolite are brighter in image (B). Thus it is evident that beam-hardening artifact in image (B) was not confined strictly to edge of the PVC casing, but was a continuous feature within the saprolite as well. Also, y-intersection of fractures just to upper-left of center (indicated by arrows) appears discontinuous in software-corrected image (B). Sample courtesy of Dr. Gerylenn Moline, Oak Ridge National Laboratory.

attenuating enough that beam hardening is noticeable unless the sample is quite small. Furthermore, higher-energy beams are less sensitive to attenuation contrasts in materials, and thus may not provide sufficient differentiation between features of interest. Another

possible strategy is to pre-harden (or post-harden) the X-ray beam by passing it through an attenuating filter before or after it passes through the scanned object (Fig. 5C). Filters are normally flat or shaped pieces of metal such as copper, brass or aluminum. The drawback

to beam filtration is that it typically degrades the X-ray signal at all energies to some degree, thus leading to greater image noise unless longer acquisition times are used. It is also characteristically only partially effective. Another method is to employ a wedge calibration using a material of similar attenuation properties to the object (Fig. 5D), as discussed above. To be effective, the wedge material should be cylindrical, and the scanned object should either be cylindrical or packed in an attenuating material (ideally the wedge material) to achieve an overall cylindrical form. If the latter is necessary, images may be noisier because of the additional X-ray attenuation caused by the packing material. The wedge material in the images also commonly interferes with 3-D analysis of the object of interest, in which case it must be eliminated during image processing.

Beam hardening is characteristically more difficult to alleviate at the data-processing stage, and such measures are usually available only in special circumstances. If the scanned object is materially uniform, a correction can be applied to the raw scan data that converts each reading to a non-beam-hardened equivalent before reconstruction takes place; unfortunately, the requirement of uniformity is more often met in industrial applications than geological ones. If the object is cylindrical and fairly uniform (i.e., a rock core), it may be possible to construct an after-the-fact wedge correction by compiling a radial average of CT values for a stack of slices. A Fourier filter that removes long-wavelength variations in CT value has also been effective in some circumstances.

4.2. Ring artifacts

Ring artifacts occur in third-generation scanning, appearing as full or partial circles centered on the rotational axis (Fig. 5A). They are caused by shifts in output from individual detectors or sets of detectors, which cause the corresponding ray or rays in each view to have anomalous values; the position of a ring corresponds to the area of greatest overlap of these rays during reconstruction. A number of factors can cause such a shift, all of which have their basis in detectors responding differently to changes in scanning conditions. Some factors, such as change in temperature or beam strength, can be overcome by carefully controlling experimental conditions or by frequent recalibrations. A more problematic source of detector divergence is differential sensitivity to varying beam hardness. If the detector response calibration (gain or wedge) is taken through air, the relative response of the detectors can change if the hardness of the X-ray beam is sufficiently affected by passage through the scanned object. If the object is uneven then different views can reflect different degrees of hardening, in which case only partial rings may occur, possibly obscuring their nature as artifacts.

Because of their link to beam hardening, ring artifacts can be addressed at the scanning stage with many of the same methods: by use of a filtered or sufficiently high-energy X-ray beam, or employing a wedge calibration through a material of similar attenuating properties to the scanned object.

Ring artifacts are somewhat more amenable to software remedies than beam hardening. A series of anomalous readings from a single detector appears on a sinogram as a vertical line, and thus it can potentially be detected and removed before reconstruction. Similarly, a reconstructed image can be converted to polar coordinates, vertical lines detected and removed, and converted back (Fig. 5B). A drawback of these strategies, particularly the latter, is that any roughly linear feature in the scanned object that is tangential to a circle centered on the rotational axis may be erased, blurred, or otherwise altered, even if it does not coincide with a ring. This can constitute a serious flaw in some applications, such as detecting sutures in fossils or tracing fractures.

In second-generation scanning, readings from an anomalous detector traverse the entire scan subject, so no rings are developed. Instead, detector drift is manifested by increased image noise.

4.3. Other artifacts

A variety of other artifacts can arise in certain situations. If a highly attenuating object is noncircular in cross-section, streaks that traverse the longest axes of the object can occur. For example, a scanned cube of a dense material may have dark streaks connecting opposite corners. These streaks can intensify ring artifacts where they overlap, making remediation more difficult. If the scanned material includes features that are of much higher density than the surrounding matrix, a “starburst” artifact can form in which bright streaks emanate from the object for a short distance into nearby material, potentially obscuring features. In several instances we have found that fossils have been repaired with steel pins, resulting in severe artifacts. Similar artifacts have been caused by crystals of sulfide or oxide minerals.

4.4. Partial-volume effects

Because each pixel in a CT image represents the attenuation properties of a specific material volume, if that volume is comprised of a number of different substances then the resulting CT value represents some average of their properties. This is termed the *partial-volume effect*. Furthermore, because of the inherent resolution limitations of X-ray CT, all material boundaries are blurred to some extent, and thus the material in any one voxel can affect CT values of surrounding voxels. Although these factors can make CT data more

problematic to interpret quantitatively, they also represent an opportunity to extract unexpectedly fine-scale data from CT images. For example, medical CT data have long been used to trace two-phase fluid flow in soil and sedimentary rock cores (Wellington and Vinegar, 1987; Withjack, 1988), even though the fluids themselves appear only as subtle attenuation changes in the matrix they are passing through. Partial-volume effects have also been used to measure crack sizes in crystalline rocks (Johns et al., 1993) and pores in soil columns (Peyton et al., 1992) down to a scale that is considerably finer than even the pixel dimensions.

The interpretation of CT values in voxels containing multiple components is not necessarily straightforward. Wellington and Vinegar (1987) utilize the approximation that the CT value in a voxel containing two components is equal to a linear combination of the CT values of the two end-members according to their volumetric proportions, which provides a reasonable solution if their attenuation values are fairly close (Pullan et al., 1981). If the end-member attenuation values are far apart, as is the case for rock and void space, significant errors of 10% or more can result from this approximation if their boundary is nearly parallel with the scan plane. However, in most cases where randomly oriented voids are studied, this error is significantly lower, and is commonly neglected without large consequence (Johns et al., 1993; Kinney et al., 1993; Wellington and Vinegar, 1987).

An example of the possible utility of partial-volume effects is shown in Fig. 6. A core of limestone from the lower Ismay member of the Paradox Formation was scanned and subsequently cut for petrographic analysis. Individual fractures that appear on the scan were measured petrographically and found to have widths that were significantly smaller than the pixel dimensions. The fracture width can be estimated using partial-volume calculations similar to those used by Johns et al. (1993), although at least one additional step is required to take fracture dip into account.

5. Optimization

Medical diagnostic CT has in many instances become a routine procedure, owing primarily to the fact that there are a limited number of truly different scanning subjects. Conversely, the wide variety of different materials and resolution requirements for geological investigations generally requires the development of specialized scanning procedures, and invariably case-by-case selection of scanning parameters. In general, the objective of optimization is to maximize the contrast between features of interest while minimizing or eliminating artifacts that can interfere with analysis.

When planning a scanning project, the first task is to identify the imaging objectives; these in turn can help

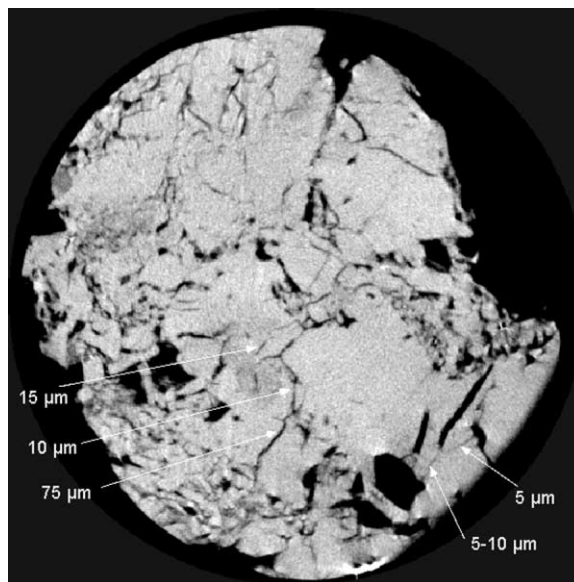


Fig. 6. 100- μ m slice through fractured limestone from lower Ismay member of Paradox Formation. Scan field of view is 21.5 mm, and individual pixels are 42 μ m on a side. After scanning entire volume, sample was cut and fractures were measured in thin section. Fractures are visible despite being considerably thinner than pixel width, because of partial volume effects. Sample and measurements courtesy of Dr. Brenda Kirkland, University of Texas at Austin.

define the necessary image resolution, slice thickness, and attenuation discrimination. These requirements guide decisions about the optimal scanning parameters, including: source–detector combination; scanning mode; X-ray energy, intensity, and spot size; beam filtration, if any; whether the sample should be scanned in air or packed; and wedge material.

We provide here an example of CT as an adaptive process in which images were progressively improved by refining scanning technique. The scanned object was a diamondiferous eclogite from Yakutia, Russia. The major phases in the rock are clinopyroxene and garnet, with accessory diamond and sulfide. Fig. 7a is an initial 50- μ m thick scan using the ultra-high-resolution system with X-rays at 200 keV and no other sample preparation or beam modification; it is essentially a scan with parameters selected to produce maximum penetration and signal strength, with no regard for mineralogy (i.e., with “everything turned up all the way”). The scan suffers from severe beam hardening, and although clinopyroxene, garnet and sulfide are fairly easy to distinguish, one cannot confidently identify diamond, even though one crystal could be seen on the edge of the sample in this plane. By evaluating the relative attenuation characteristics of diamond and clinopyroxene, it was recognized that they have nearly indistinguishable attenuation coefficients at high X-ray

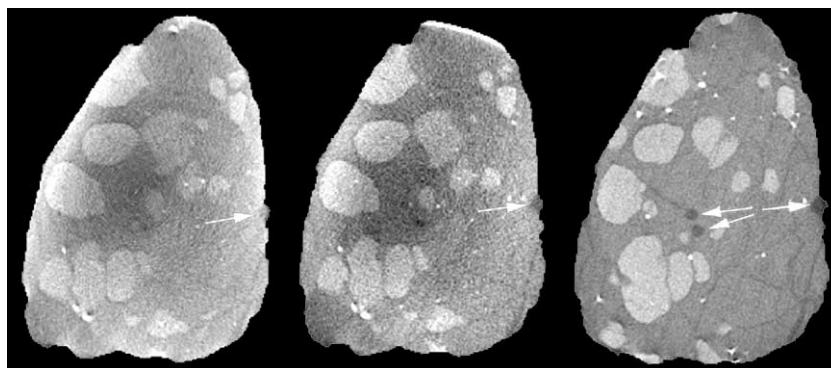


Fig. 7. Three scans of diamondiferous eclogite showing effects of successive improvements of scanning methodology. Phases present, in order of increasing grayscale, are diamond, clinopyroxene, garnet, and sulfide. Scanning conditions discussed in text. Sample approximately 50 mm in long dimension. Sample courtesy of Dr. Larry Taylor and Dr. Randall Keller, University of Tennessee at Knoxville.

energies (>150 keV), but diverge greatly at lower energies because of the low mean atomic number of diamond. To help confine the X-ray energy spectrum to a more useful range while attempting to diminish beam hardening, the scan in Fig. 7b was acquired with X-rays set at 100 keV and pre-filtered with a 1/8" brass plate. The diamond at the edge of the sample is now more easily distinguished, and the beam hardening is slightly diminished by prefiltering. However, these two measures also produced greater image noise. Optimal imagery was obtained through use of a wedge calibration: the sample was packed in a cylindrical container with finely ground garnet powder, the calibration was taken through pure garnet powder, and the brass filter was removed to increase total X-ray intensity (Fig. 7c). The mixture of garnet and air in the powder make it a close match for the attenuating characteristics of clinopyroxene, and thus the calibration was able to eliminate the beam-hardening artifact. Because the wedge material also allowed the use of a higher gain in the video system during calibration, counting statistics were also improved. The results are remarkable; not only is the external diamond even more clearly visible, but previously invisible diamonds in the center of the image have become apparent, along with a network of alteration zones that may be related to the diamonds' origin.

6. Visualization of CT images

The product of a complete X-ray CT scan is a three-dimensional matrix of relative attenuation values, sometimes called a "data brick". The most productive way of visualizing such data depends on the scientific application. In many cases, particularly paleontological studies, two-dimensional slices through the data along three sets of orthogonal planes (coronal, sagittal, horizontal) are the best way to inspect skeletal structures. The reason

for this is partly traditional, as these planes have long been used in serial-sectioning studies. In most cases, however, additional insight can be gained by creating a three-dimensional representation. We discuss here some current approaches to 3-D visualization of X-ray CT data, and in the next section present examples from various studies.

Two primary techniques exist for creating three-dimensional images from CT data: *isocontouring* and *volume rendering*. Isocontouring is the more widely familiar of the two; it consists of defining one or more surfaces (isosurfaces) that mark the boundaries of the object(s) of interest in the scan. In most cases these boundaries are assumed to correspond to a certain CT value, and thus the isocontours mark these constant-CT-value surfaces in the volume, in much the same manner as contours on a topographic map mark lines of constant elevation. As is analogous to the case of constructing topographic maps from gridded data, isocontour positions are interpolated among the data points, and thus the surfaces are defined on a sub-pixel scale. In volume rendering each voxel in the volume is assigned a red–green–blue color (or grayscale) and an opacity, based on its CT number. By setting the opacity of some voxels to zero, they can be made invisible, thus allowing the observer to "see through" them to nontransparent materials of interest.

These two techniques are useful in different circumstances. In most cases, we have found volume rendering to be better suited to CT imagery, because a larger range of information is available to be included in an image. In particular, if two materials have overlapping CT values because of internal textures, image noise, or artifacts, defining an isocontour between them becomes arbitrary and hazardous. On the other hand, volume rendering allows the viewer to distinguish the two visually, based on their changes in average CT value or textural differences. Also, isocontouring large data sets can be

more demanding on memory and processing power than volume rendering, and in many cases a detailed data set must be considerably reduced and simplified before an isocontour can be calculated and rendered.

Nevertheless, isocontouring is frequently a desirable goal because of the crisper images and more detailed surface information and volumetric measurements it can provide. To be effective for CT data, an additional step called *segmentation* is generally necessary to separate features of interest based on more robust criteria than simply the CT values. Some steps that can aid segmentation include noise reduction, edge enhancement and tracking, and region growing (Glenn et al., 1981). The field is continuing to develop rapidly, incorporating a wide variety of computational and statistical techniques (Glasbey and Horgan, 1995). If quantitative measurements are desired from X-ray CT data, additional segmentation steps that take partial-volume effects into account may be required. For example, Peyton et al. (1992) found that sizes of pores in soil as imaged by medical CT are not directly proportional to the actual pore sizes, due to blurring and partial-volume effects, which cause different-sized pores to be manifested with different CT values. Thus, to establish pore size they use an iterative procedure based on scanned standards that link pore sizes to cutoff CT values. Another complication inherent in isosurfacing is that the CT value marking the boundary of an object will change depending on the character of adjacent materials. For example, if a garnet has a CT value of 3000 and is adjacent to both quartz with a CT value of 2000 and air with a CT value of 0, the appropriate CT value marking its boundary will be roughly 2500 on the side facing quartz and 1500 on the side facing air. In many cases the resulting data corruption will be slight, particularly if the data are high-resolution, but it should be considered when evaluating data precision.

7. Examples of geological applications

In this section we summarize the results from some of the geological studies carried out at the UT High-Resolution X-ray CT Facility. Most of the figures in this section have accompanying animations viewable on the CD that supplements this volume or on the *Computers & Geosciences* Internet site.

7.1. Quantitative analysis of metamorphic textures

The original stimulus for establishment of the UT high-resolution X-ray CT facility was the recognition that 3-D CT data on the sizes and locations of crystals permit quantitative analysis of textures. In particular, such data permit discrimination between competing hypotheses for the atomic-scale mechanisms controlling the growth of metamorphic porphyroblasts. The result

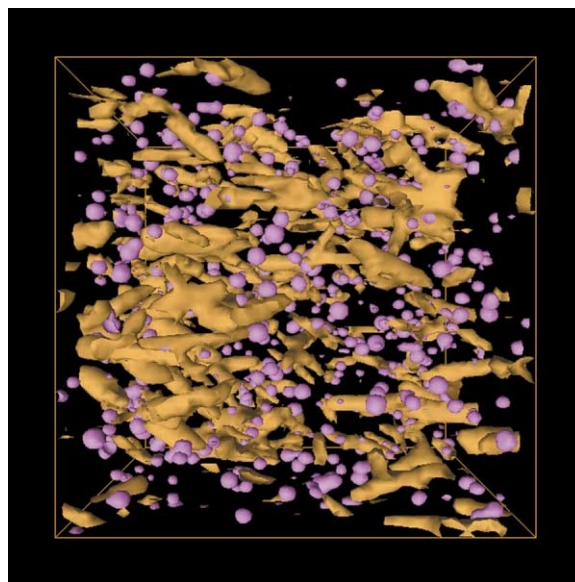


Fig. 8. Isosurface image of garnet (violet) and staurolite (yellow–brown) in schist from Picuris Mountains, New Mexico. Sizes and spatial positions of porphyroblasts as revealed by X-ray CT can be used to determine whether there is any ordering among them, which may indicate that during nucleation and growth crystals were surrounded by diffusionally depleted zones that restricted further nucleation in their vicinity. Image bounding box is approximately $45 \times 45 \times 42$ mm.

of initial forays into this field demonstrated that reaction kinetics limited by rates of intergranular diffusion were common for garnet porphyroblasts in regionally metamorphosed rocks (Carlson and Denison, 1992; Denison and Carlson, 1997; Denison et al., 1997). Numerical simulations of such processes (Carlson et al., 1995), constrained by the X-ray CT data, allowed first-ever estimates of critical kinetic parameters such as the absolute rates of garnet nucleation and of intergranular diffusion of aluminum (the transport of which is rate-limiting). Compositional studies based on serial sectioning guided by the CT data (Chernoff and Carlson, 1997, 1999) demonstrated the importance of this reaction control: sluggish intergranular diffusion appears to account for the observation that Ca and many trace elements in some metamorphic rocks fail to equilibrate at the thin-section scale during garnet growth, severely restricting the confidence that can be placed in thermobarometric methods that assume otherwise. Further studies are being conducted in pursuit of deeper understanding of reaction processes at subcrystalline length scales, including analysis of porphyroblasts other than garnet and rocks metamorphosed under a wider range of temperature, pressure, strain rate, and fluid-flow conditions.

Fig. 8 shows an isosurface rendering of garnet and staurolite in a pelitic schist from the Picuris Mountains,

New Mexico. The markedly different attenuation properties of the two phases combined with the homogeneity of the micaceous matrix in this sample made their separation fairly straightforward, but a number of steps were required to produce the imagery shown. First, a subset of the original data was taken and re-scaled from 512 to 128 pixels on a side. This data set was then used to construct the set of isocontours for garnet, the phase with the highest CT value. Because an isocontour enclosing the CT value of staurolite crystals would also enclose garnet, in order to render the staurolite crystals, all of the garnets had to be erased from the original data set. Furthermore, because of blurring and partial volume effects, the garnet boundaries have CT values that overlap with the staurolites, so the material immediately adjacent to the garnets had to be deleted as well. The staurolite isosurfaces were calculated from the modified data set, and the two sets of isosurfaces were then superposed.

7.2. Metasomatic processes in the Earth's mantle and the origin of diamond

The nature and extent of mantle metasomatism and the origin of diamond — fundamental enigmas in mantle petrology — have been addressed by complete 3-D characterization of textural relationships in extraordinary diamondiferous eclogites from Udachnaya, Siberia (Keller et al., 1999). These rare specimens are problematic to study by petrographic means, in part

because of the extreme difficulty of sawing through diamonds. Furthermore, two-dimensional analysis may miss crucial textural features relating diamonds to fractures and other phases. CT imagery revealed that none of the diamonds in the specimen are completely enclosed in either garnet or clinopyroxene, but instead all are spatially associated with a 3-D network of alteration zones that penetrate the specimen (Fig. 9). The implication is that the diamond postdates formation of the eclogitic assemblage, and most likely originated during a metasomatic event responsible for localized alteration along subplanar zones; this hypothesis is now being tested further by means of chemical and isotopic analysis of the disaggregated specimen.

The images in Fig. 9 were constructed using volume rendering instead of isosurfacing. Each phase is rendered transparent, partially transparent or opaque to allow inspection of different textural features. Except for removal of the wedge material, this rendering did not require any processing or enhancement of the original images.

7.3. Melt generation, segregation, and migration in a lodranite

Initial curatorial slabbing of the lodranite meteorite GRA95209 produced the surprising discovery of a large region of metal segregated from the mixed silicate-metal matrix. X-ray CT was used to determine, nondestructively, the geometry of this metal segregation (Carlson

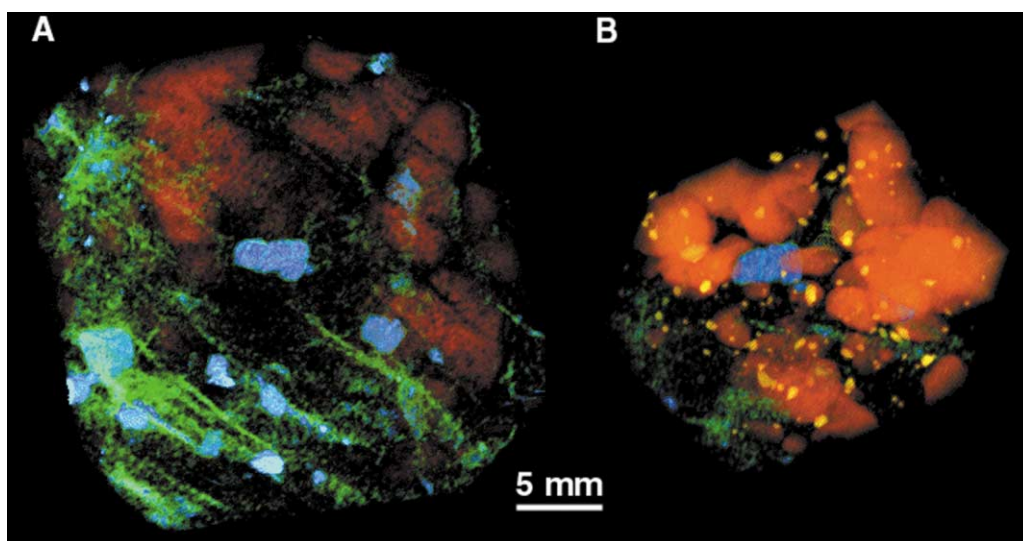


Fig. 9. Volume renderings of diamondiferous eclogite from Yakutia, Russia, based on scans such as those shown in Fig. 7C. Images reveal diamond (blue), sulphides (yellow) and garnet (red); clinopyroxene that comprises most of specimen has been rendered entirely transparent except for network of alteration zones (green) that intersects all of the diamonds. A. Portion of sample with alteration zones highlighted. B. Smaller subset with garnet and sulphide phases enhanced. Sample courtesy of Dr. Larry Taylor and Dr. Randall Keller, University of Tennessee at Knoxville.

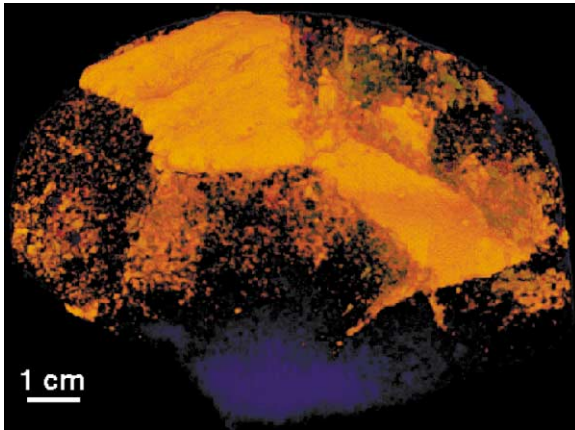


Fig. 10. Volume rendering of distribution of metal in lodranite meteorite GRA95209. Long dimension of sample is approximately 80 mm. Sample courtesy of Dr. Marilyn Lindstrom, NASA, and Dr. Tim McCoy, Smithsonian Institution.

and McCoy, 1998; McCoy and Carlson, 1998). A large slab of metal was found to be present along the exterior surface of much of the specimen (obscured beneath a fusion crust), extending into its interior, connected to several veins and stringers of metal within the matrix; the matrix was seen to include metal-poor silicate-rich regions (Fig. 10). The coalescing veins and dikelets revealed in 3-D by X-ray CT are readily interpreted as melt-migration pathways, and measurements from CT data of the relative volumes of metal and metal-depleted matrix permit mass-balance calculations that rule out a completely local origin for the melt. The images therefore record a complicated and intriguing picture of melt generation and migration in the lodranite parent body, a primitive planetesimal that is one of the best existing models for processes occurring during core–mantle segregation in the terrestrial planets.

7.4. Characterization of porosity in reservoir limestones

X-ray CT imagery of rock porosity can be used in a variety of applications, from qualitative characterization of porosity types and fabrics (Beall et al., 1996; Gournay and Kirkland, 1998) to quantitative description of pore networks for examination and modeling of fluid-flow characteristics. Pore geometry, pore dimensions, pore-throat sizes and surface roughness all affect flow. Pore-to-pore-throat geometries may affect migration of hydrocarbons and are certainly significant in production of hydrocarbons from the reservoir. X-ray CT data have been used to examine four types of porosity in reservoir limestones: fracture porosity, which is the most important for flow and interconnection of other types of porosity; moldic (intra-particle) porosity; inter-particle porosity; and vuggy porosity. The imagery is being used

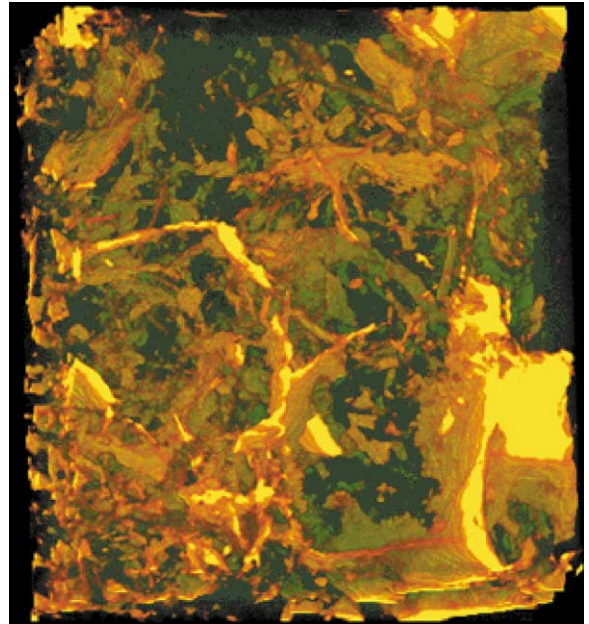


Fig. 11. Volume rendering image of fracture network in reservoir limestone from lower Ismay formation of Paradox Formation, west Texas. Reconstruction is approximately 15 mm wide. Sample courtesy of Dr. Brenda Kirkland, University of Texas at Austin.

to construct three-dimensional permeability-network maps to help link the geometric characteristics of the pore network to its flow properties. Such maps may help identify regions of suspected laminar versus turbulent flow that could affect the diagenetic processes governing the formation of porous hydrocarbon reservoirs and aquifers.

An example image from a fractured limestone is shown in Fig. 6, and a 3-D volume-rendering reconstruction of the stacked images to reveal the fractures and pore spaces is shown in Fig. 11. An isosurface rendering of the original data to show the fractures would be problematic, because as discussed above there is no single appropriate CT value that marks the rock-void boundary across the size range of fractures present. Volume rendering allowed us to circumvent this difficulty by showing different-sized fractures in different colors and intensities. In this case, small fractures are shown in semitransparent red, and large, open fractures appear as bright yellow with red boundaries.

7.5. Structural origin and 3-D extent of banding in scleractinian corals

Annual banding in scleractinian corals makes them useful indicators of temperature and chemical conditions through time in coral reefs, thus allowing them to

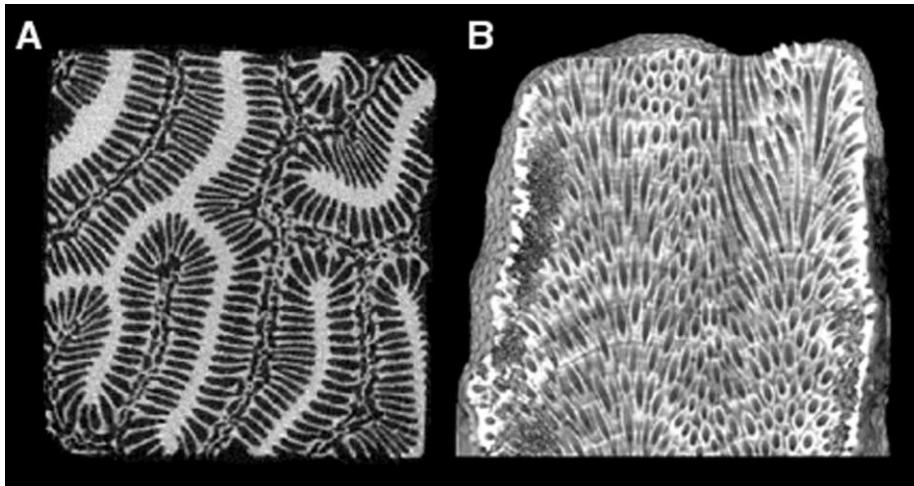


Fig. 12. A. X-ray CT image of 25-cm cut cube of coral *Diploria strigosa* used to study structural elements responsible for density banding. Slice thickness is 100 μ m. High-density bands correlate with thickened septa and tightly organized and thickened columella. Sample courtesy of Dr. Richard Dodge and Kevin Helmle of Nova Southeastern University. B. Three-dimensional pattern of annual growth banding in sample of coral *Montastrea annularis*. Sample is approximately 90 mm wide. Sample courtesy of Dr. Judy Lang and Dr. Lynton Land, University of Texas at Austin.

serve as precise long-term climate records (Knutson et al., 1972; Swart et al., 1996). This banding is commonly imaged using traditional projection X-radiography, which can locate the bands in cut slabs of coral. X-ray CT offers a number of opportunities to refine understanding and implementation of these techniques. Ultra-high-resolution CT has been used to inspect in detail the geometrical characteristics of the bands in *Diploria strigosa* (Fig. 12A) to determine the structural elements responsible for them (Helmle, 1998). Results indicate that banding architecture varies across coral taxa.

High-resolution X-ray CT can also be used to ensure that sampling techniques properly account for the full three-dimensional variability of coral banding. Sampling is commonly done using a coring drill positioned normal to the coral surface. A complete scan of coral *Montastrea annularis* (Fig. 12B) reveals that these bands may not remain perpendicular to this surface because of variations in the relative growth rates of different parts of the coral through time. Visualization of these features can be effectively done through single images and animated series of digitally resliced data.

7.6. Skull morphology of *Kryptobataar*

The ability of high-resolution X-ray CT to image fossil interiors and exteriors profoundly increases the amount of morphological information that can be nondestructively obtained from them. Furthermore, it can also fulfill a curatorial function, as once the fossil is scanned its data can be widely disseminated. For example, under normal circumstances, to study a certain

species a paleontologist may have to travel to all of the different museums that have relevant specimens. The potential now exists to catalog museum collections and make them available on electronic media or, eventually, via the Internet.

Although most paleontologists have computers, some may not have the computational resources and expertise required to efficiently visualize and manipulate the tens to hundreds of megabytes of data that CT can produce for a single specimen. Thus, distribution of CT data generally includes preparation of images and animations for trouble-free viewing and analysis. Examples of such data processing include reslicing the data along the traditional orthogonal planes used for morphological analysis and constructing three-dimensional renderings.

Fig. 13 shows an example of some rendering and data-distribution techniques for a high-resolution scan of a specimen of *Kryptobataar dashzevegi*, from the late Cretaceous Djadokhta Formation, Ukhua Tolgod, Mongolia. Fig. 13A shows a volume rendering of the *Kryptobataar* skull with part of it digitally removed to reveal the internal features at the slice plane. The ability to simultaneously display the internal structure and external form of the skull helps in the identification of individual skeletal elements and their relation to each other. Figs. 13B and C are three-dimensional images of the entire skull created using volume rendering and isosurfacing, respectively. The isosurface shows the details of the skull surface more clearly, but the volume rendering allows for better differentiation between skull and matrix, and reproduces more faithfully the state of the original specimen.

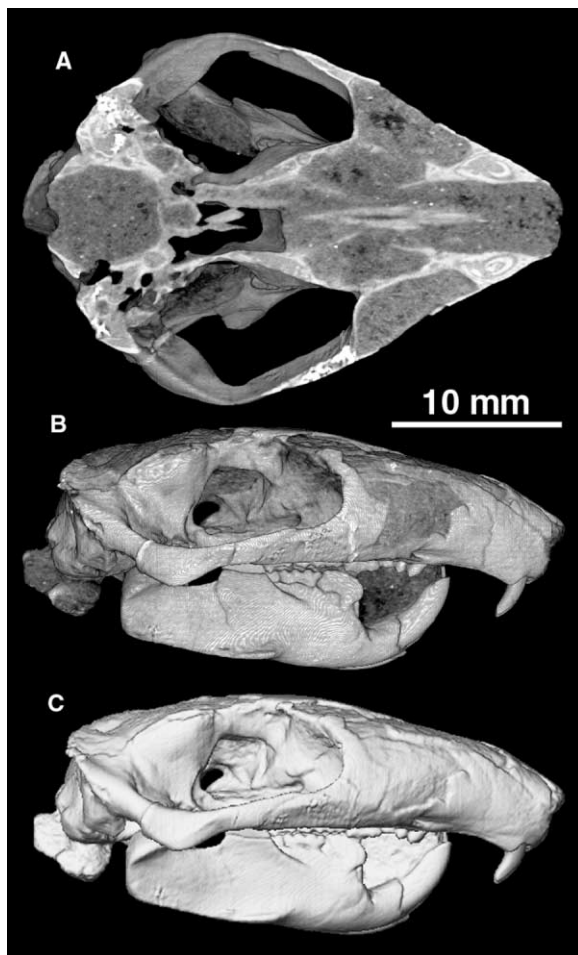


Fig. 13. Three-dimensional reconstructions based on X-ray CT data of skull of *Kryptobataar*. Skull is 29 mm long. (A) volume rendering of skull from above, with cutaway showing internal structure; (B) volume rendering of skull; (C) isosurface rendering of skull. Sample courtesy of Dr. Guillermo W. Rougier, University of Louisville.

8. Summary

High-resolution X-ray CT is ideally suited to many geological applications, and its potential is only beginning to be explored. We hope that the overview and examples given here can provide inspiration for new investigations that will benefit from further utilization of this breakthrough technology.

Acknowledgements

The University of Texas at Austin High-Resolution X-ray CT Facility was created with support from the W.M. Keck Foundation, the National Science Founda-

tion (NSF EAR-9406258; NSF EAR-9816020), and the Geology Foundation of the University of Texas. Many of the images and animations presented here were created by Dr. Cambria Denison, who also participated in the development of many of the scanning techniques described and employed. We thank two anonymous referees for constructive comments, as well as editors R. Marschallinger and S. Johnson.

References

- Amos, C.L., Sutherland, T.F., Radzjewski, B., Doucette, M., 1996. A rapid technique to determine bulk density of fine-grained sediments by X-ray computed tomography. *Journal of Sedimentary Research* 66 (5), 1023–1024.
- Anderson, S.H., Peyton, R.L., Wigger, J.W., Gantzer, C.J., 1992. Influence of aggregate size on solute transport as measured using computed tomography. *Geoderma* 53, 387–398.
- Arnold, J.R., Testa, J.P.J., Friedman, P.J., Kambic, G.X., 1982. Computed tomographic analysis of meteorite inclusions. *Science* 219, 383–384.
- ASTM, 1992. Standard Guide for Computed Tomography (CT) Imaging, ASTM Designation E 1441-92a. In: 1992 Annual Book of ASTM Standards, Section 3 Metals Test Methods and Analytical Procedures. ASTM, Philadelphia, pp. 690–713.
- Bauer, R.L., Ketcham, R.A., Denison, C., Carlson, W.D., 1998. X-ray computed tomography (CT) imaging of spiral inclusion trails and the external morphology of garnet porphyroblasts. *Eos* 79 (17), 357.
- Beall, J.L., Gordon, I.T., Gournay, J.P., Kirkland, B.L., White, J.V., 1996. Analysis of porosity in lower Ismay phylloid algal packstone using high-resolution computed X-ray tomography. *American Association of Petroleum Geologists, Annual Meeting Abstracts* 5, 13.
- Brown, M.A., Brown, M., Carlson, W.D., Denison, C., 1999. Topology of syntectonic melt flow networks in the deep crust: inferences from three-dimensional images of leucosome geometry in migmatites. *American Mineralogist* 84, 1793–1818.
- Carlson, W.D., Denison, C., 1992. Mechanisms of porphyroblast crystallization: results from high-resolution computed X-ray tomography. *Science* 257, 1236–1239.
- Carlson, W.D., Denison, C., Ketcham, R.A., 1995. Controls on the nucleation and growth of porphyroblasts: kinetics from natural textures and numerical models. *Geological Journal* 30, 207–225.
- Carlson, W.D., McCoy, T.J., 1998. High-resolution X-ray computed tomography of lodranite GRA 95209. In: *Lunar and Planetary Science, Vol. XXIX, CD-ROM*. Lunar and Planetary Science Institute, Houston.
- Chen, M.-R., Hinkley, R.E., Killough, J.E., 1996. Computed tomography imaging of air sparging in porous media. *Water Resources Research* 32 (10), 3013–3024.
- Chernoff, C.B., Carlson, W.D., 1997. Disequilibrium for Ca during growth of pelitic garnet. *Journal of Metamorphic Geology* 15 (4), 421–438.
- Chernoff, C.B., Carlson, W.D., 1999. Trace element zoning as a record of chemical disequilibrium during garnet growth. *Geology* 27 (6), 555–558.

- Cifelli, R.L., Muizon, C.D., 1998a. Marsupial mammal from the Upper Cretaceous North Horn Formation, central Utah. *Journal of Paleontology* 72, 532–537.
- Cifelli, R.L., Muizon, C.D., 1998b. Tooth eruption and replacement pattern in early marsupials. *Comptes Rendus, Académie des Sciences* 326, 215–220.
- Cifelli, R.L., Rowe, T.B., Luckett, W.P., Banta, J., Reyes, R., Howes, R.I., 1996. Fossil evidence for the origin of the marsupial pattern of tooth replacement. *Nature* 379, 715–718.
- Coker, D.A., Torquato, S., Dunsmuir, J.H., 1996. Morphology and physical properties of Fontainebleau sandstone via a tomographic analysis. *Journal of Geophysical Research* 101 (B8), 17,497–17,506.
- Conroy, G.C., Vannier, M.W., 1984. Noninvasive three-dimensional computer imaging of matrix-filled fossil skulls by high-resolution computed tomography. *Science* 226, 456–458.
- Denison, C., Carlson, W.D., 1997. Three-dimensional quantitative textural analysis of metamorphic rocks using high-resolution computed X-ray tomography: Part II. Application to natural samples. *Journal of Metamorphic Geology* 15 (1), 45–57.
- Denison, C., Carlson, W.D., Ketcham, R.A., 1997. Three-dimensional quantitative textural analysis of metamorphic rocks using high-resolution computed X-ray tomography: Part I. Methods and techniques. *Journal of Metamorphic Geology* 15 (1), 29–44.
- Flannery, B.P., Deckman, H.W., Roberge, W.G., D'Amico, K.L., 1987. Three-dimensional X-ray microtomography. *Science* 237, 1439–1444.
- Fourie, S., 1974. The cranial morphology of *Thrinaxodon liorhinus* Seeley. *Annals of the South African Museum* 65, 337–400.
- Glasbey, C.A., Horgan, G.W., 1995. *Image Analysis for the Biological Sciences*. Wiley, New York, 218 pp.
- Glenn, W.V., Harlow, C.A., Dwyer, S.J.I., Rhodes, M.L., Parker, D.L., 1981. Image manipulation and pattern recognition. In: Newton, T.H., Potts, D.G. (Eds.), *Technical Aspects of Computed Tomography*. Mosby, St. Louis, pp. 4326–4354.
- Gournay, J.P., Kirkland, B.L., 1998. Fabric development in phylloid algal bioherms. *American Association of Petroleum Geologists, Annual Meeting Abstracts* 7.
- Haubitz, B., Prokop, M., Dohring, W., Ostrom, J.H., Wellenhofer, P., 1988. Computed tomography of Archaeopteryx. *Paleobiology* 14 (2), 206–213.
- Heijs, A.W.J., De Lange, J., Schoute, J.F.T., Bouma, J., 1995. Computed tomography as a tool for non-destructive analysis of flow patterns in macroporous clay soils. *Geoderma* 64, 183–196.
- Helmle, K., 1998. Relationships between skeletal architecture and density banding in the reef coral *Diploria strigosa* from X-radiography, X-ray computed tomography, and image analysis techniques. *Oceanographic Center, M.S. Nova Southeastern University, Dania, FL*, 86 pp.
- Hendee, W.R., 1979. *Medical Radiation Physics*. 2nd edn. Year Book Medical Publishers, Chicago, 517 pp.
- Johns, R.A., Steude, J.S., Castanier, L.M., Roberts, P.V., 1993. Nondestructive measurements of fracture aperture in crystalline rock cores using X-ray computed tomography. *Journal of Geophysical Research* 98 (B2), 1889–1900.
- Keller, R.A., Taylor, L.A., Snyder, G.A., Sobolev, V.N., Carlson, W.D., Bezborodov, S.M., Sobolev, N.V., 1999. Detailed pull-apart of a diamondiferous eclogite xenolith: Implications for mantle processes during diamond genesis. In: Gurney, J.J., Gurney, J.L., Pascoe, M.D., Richardson, S.H. (Eds.), *Proc. 7th International Kimberlite Conf., Vol. 1*, National Printers, So. Afr., pp. 397–412.
- Kinney, J.H., Breuning, T.M., Starr, T.L., Haupt, D., Nichols, M.C., Stock, S.R., Butts, M.D., Saroyan, R.A., 1993. X-ray tomographic study of chemical vapor infiltration processing of ceramic deposits. *Science* 260, 782–789.
- Knutson, D.W., Buddemeier, R.W., Smith, S.V., 1972. Coral chronometers: seasonal growth bands in reef corals. *Science* 177, 270–272.
- Kretz, R., 1966. Grain size distribution for certain metamorphic minerals in relation to nucleation and growth. *Journal of Geology* 74, 147–173.
- Kretz, R., 1969. On the spatial distribution of crystals in rocks. *Lithos* 2, 39–66.
- Kretz, R., 1993. A garnet population in Yellowknife schist, Canada. *Journal of Metamorphic Geology* 11, 101–120.
- Kuebler, K.E., McSween, H.Y., Carlson, W.D., Hirsch, D., 1999. Sizes and masses of chondrules and metal-troilite grains in ordinary chondrites: possible implications for nebular sorting. *Icarus* 141, 96–106.
- Le Calvez, J., Vendeville, B.C., 1999. X-ray tomographic analysis of a physical experiment of salt tongue remobilization during sedimentation. *AAPG International Conference and Exhibition Program*, 31.
- Markowicz, A.A., 1993. X-ray physics. In: Van Grieken, R.E., Markowicz, A.A. (Eds.), *Handbook of X-ray Spectrometry*. Marcel Dekker, New York, pp. 1–28.
- McCoy, T.J., Carlson, W.D., 1998. Opaque minerals in GRA 95209 lodranite: a snapshot of metal segregation. In: *Lunar and Planetary Science XXIX, CD-ROM*. Lunar and Planetary Science Institute, Houston.
- Moline, G.R., Knight, C.R., Ketcham, R.A., 1997. Laboratory measurement of transport processes in a fractured limestone/shale saprolite using solute and colloid tracers. *Geological Society of America, Abstracts with Programs* 29, 370.
- Newton, T.H., Potts, D.G., 1981. *Technical Aspects of Computed Tomography*, Vol. 5. Mosby, St. Louis, 615 pp.
- Ogasawara, Y., Ando, T., Carlson, W.D., Ketcham, R.A., 1998. Serial-grinding and X-ray CT techniques for 3D observation of rock textures — an example of magmamingled rock from Colorado. *Eos* 79 (17), 356.
- Orsi, T.H., Anderson, A.L., 1995. X-ray computed tomography of macroscale variability in sediment physical properties, offshore Louisiana. In: John, C.J., Byrnes, M.R. (Eds.), *Transactions of the Forty-Fifth Annual Convention of the Gulf Coast Association of Geological Societies*. Gulf Coast Association of Geological Societies, New Orleans, pp. 475–480.
- Orsi, T.H., Edwards, C.M., Anderson, A.L., 1994. X-ray computed tomography: a nondestructive method for quantitative analysis of sediment cores. *Journal of Sedimentary Research, Section A: Sedimentary Petrology and Processes* 64 (3), 690–693.
- Peyton, R.L., Haeffner, B.A., Anderson, S.H., Gantzer, C.J., 1992. Applying X-ray CT to measure macropore diameters in undisturbed soil cores. *Geoderma* 53, 329–340.
- Proussevitch, A., Ketcham, R.A., Carlson, W.D., Sahagian, D., 1998. Preliminary results of X-ray CT analysis of Hawaiian vesicular basalts. *Eos* 79 (17), 360.

- Pullan, B.R., Ritchings, R.T., Isherwood, I., 1981. Accuracy and meaning of computed tomography attenuation values. In: Newton, T.H., Potts, D.G. (Eds.), *Technical Aspects of Computed Tomography*. Mosby, St. Louis, pp. 3904–3917.
- Ramachandran, G.N., Lakshminarayanan, A.V., 1970. Three-dimensional reconstruction from radiographs and electron micrographs: application of convolutions instead of Fourier transforms. *Proceedings of the National Academy of Science* 68, 2236–2240.
- Rowe, T., 1996. Coevolution of the mammalian middle ear and neocortex. *Science* 273, 651–654.
- Rowe, T.B., Carlson, W.D., Bottdorf, W.W., 1993. *Thrinaxodon Digital Atlas of the Skull*, CD-ROM, 623 Mb. University of Texas Press, Austin.
- Schreurs, G., Hänni, R., 1998. 4-D analysis of analogue model experiments. *American Association of Petroleum Geologists Bulletin* 82 (10), 1965.
- Shepp, L.A., Logan, B.F., 1974. Reconstructing interior head tissue from X-ray transmissions. *IEEE Transactions on Nuclear Science* NS-21, 228–236.
- Silver, M.D., 1994. Target self-attenuation extension to the Desorby and Boyer thick-target bremsstrahlung spectrum. *Medical Physics* 21 (4), 577–579.
- Swart, P.K., Healy, G.F., Dodge, R.E., Kramer, P., Hudson, J.H., Halley, R.B., Robblee, M.B., 1996. The stable oxygen and carbon isotopic record from a coral growing in Florida Bay: a 160 year record of climatic and anthropogenic change. *Palaeogeography, Palaeoclimatology, Palaeoecology* 123, 219–237.
- Wellington, S.L., Vinegar, H.J., 1987. X-ray computerized tomography. *Journal of Petroleum Technology* 39 (8), 885–898.
- Withjack, E.M., 1988. Computed tomography for rock-property determination and fluid-flow visualization. *SPE Formation Evaluation* 3 (4), 696–704.
- Zatz, L.M., 1981. Basic principles of computed tomography scanning. In: Newton, T.H., Potts, D.G. (Eds.), *Technical Aspects of Computed Tomography*. Mosby, St. Louis, pp. 3853–3876.
- Zeng, Y., Gantzer, C.J., Peyton, R.L., Anderson, S.H., 1996. Fractal dimension and lacunarity of bulk density determined with X-ray computed tomography. *Soil Science Society of America Journal* 60, 1718–1724.
- Zinsmeister, W.J., De Nooyer, C., 1996. Computed tomography; non-destructive techniques for visualizing internal morphology of invertebrates. *Geological Society of America, Abstracts with Programs* 28 (7), 294.